Image-Based Subthalamic Nucleus Segmentation for Deep Brain Surgery with Electrophysiology Aided Refinement

Igor Varga[1(✉)], Eduard Bakstein[1,3(✉)], Greydon Gilmore[2(✉)], and Daniel Novak[1(✉)]

[1] Czech Technical University in Prague, 160 00 Prague, Czech Republic
{varhaiho,eduard.bakstein}@fel.cvut.cz
[2] Western University, Ontario, ON N6A 3K7, Canada
greydon.gilmore@gmail.com
[3] National Institute of Mental Health, 50 67 Klecany, Czech Republic

Abstract. Identification of subcortical structures is an essential step in surgical planning for interventions such as the deep brain stimulation (DBS), in which permanent electrode is implanted in a precisely defined location. For refinement of the target localisation and compensation of brain shift occurring during the surgery, intra-operative electrophysiological recording using microelectrodes is usually undertaken.

In this paper, we present a multimodal method that consists of a) subthalamic nucleus (STN) segmentation from magnetic resonance T2 images using 3D active contour fitting and b) a subsequent brain shift compensation step, increasing the accuracy of microelectrode placement localisation by the probabilistic electrophysiology-based fitting. The method is evaluated on a data set of 39 multi-electrode trajectories from 20 patients undergoing DBS surgery for Parkinson's disease in a leave-one-subject-out scenario. The performance comparison shows increased sensitivity and slightly decreased specificity of STN identification using the individually-segmented 3D contours, compared to electrophysiology-based refinement of a standard 3D atlas.

To achieve accurate segmentation from the low-resolution clinical T2 images, a more sophisticated approach, including shape priors and intensity model, needs to be implemented. However, the presented approach is a step towards automatic identification of microelectrode recording sites and possibly also an assistive system for the DBS surgery.

Keywords: Active contours · Deep brain stimulation · Surface fitting · Subthalamic nucleus

1 Introduction

Accurate identification of subcortical structures from medical images plays a vital role in the planning of stereotactic surgery in neurological diseases, such

T. Syeda-Mahmood et al. (Eds.): ML-CDS 2020/CLIP 2020, LNCS 12445, pp. 34–43, 2020.
https://doi.org/10.1007/978-3-030-60946-7_4

as the Parkinson disease (PD) or Dystonia. During the last 20 years, the DBS, targeted in the Subthalamic nucleus, has become an established treatment for late-stage treatment-resistant PD. The electrode implantation planning relies on pre-operative cranial magnetic resonance imaging (MRI) with visualisation of the target nucleus using spin-spin relaxation (T2) [8]. Further positioning of the electrode can be refined intra-operatively by the injection of exploratory electrodes and multitrajectory microelectrode-recording (MER) during surgery [4].

Currently, research studies show robust approaches to perform image segmentation of subcortical structures [12,16]. These segmentation techniques use intensity-based probabilistic models to identify individual patient's STN and support planning targets for electrode positions. However, during surgery, the target may be displaced from the planned position due to brain shift and electrode bending.

Here, we introduce a segmentation model that allows evaluation of brain shift during surgery based on the segmented STN contour and MER-based refinement. The training stage in segmentation algorithms usually requires manual labelling of the target structure volume, which requires expert knowledge and is highly time-consuming. The Active Contour Model (ACM) approaches were applied in medical image processing previously [6] as an intensity-based segmentation technique. One of our goals is to minimise labelling time, by using partial labelling of STN using just two landmark points, where the ACM will carry out adjustment of the nucleus borders based on image properties.

In the last stage, we use an electrophysiology-based model to estimate the displacement of exploratory electrodes with respect to the surgical plan and their position within STN using the model previously derived from the MRI images.

2 Methods

The approach we used can be divided into the following steps: intensity normalisation over white matter (WM), STN atlas mesh positioning and border adjustment, which results in an individual STN surface representation. A maximum-likelihood translation of this surface model is then found according to a probabilistic model of electrophysiological activity inside/outside of the nucleus.

2.1 Data

The data we used consists of 20 subjects, each of them containing:

1. Preoperative spin-lattice relaxation T1-weighted images (TE = 1.5 ms, TI = 300 ms)
2. Preoperative T2-weighted (TE = 110 ms, TR = 2800 ms) slab slices
3. Intra-operative MER recording with recording frequency 24 kHz

This group consists of subjects who underwent STN-targeted DBS therapy at the University of Western Ontario, Canada. All MRI images were recorded with a 1.5T clinical scanner (Signa 1.5T scanner, General Electric, Milwaukee,

Wisconsin, USA) two weeks prior to surgery. The slice thickness was 1.5 mm. STN was manually labelled by two landmark points: the most anterior (P1) and the most dorsal part (P2) [14].

2.2 MER Acquisition and Preprocessing

A computer-controlled microelectrode drive was mounted to the stereotactic frame (StarDrive, FHC Inc., Bowdoinham, ME), and 2–5 cannulas with tungsten microelectrodes (60 µm diameter) were lowered to 10.0 mm above the surgically planned target. Electrophysiological signals were recorded in increments of 1.00 mm (10.00 mm to 5.00 mm above the surgical target) and 0.50 *mm* (5.00 *mm* above the target until the substantia nigra reticulata was reached, marking the ventral STN border). At each recording site, data was collected for 10 s, which resulted in approximately 25–30 recordings for each microelectrode. The signals were sampled (24 kHz, 8-bit), amplified (gain: 10000) and digitally filtered (bandpass: 500–5000 Hz, notch: 60 Hz) using the Leadpoint recording station (Leadpoint 5, Medtronic).

Then, stationary segments of the electrophysiology data were first identified using the covariance method from [3], and the root-mean-square value has been calculated from the stationary segments for each signal. Next, the normalised root-mean-square values (NRMS) were calculated for each trajectory by using the first five recording positions as a reference [11]. All MER processing and fitting were performed using Matlab (MathWorks Inc., Natick, MA, USA).

2.3 MRI Data Processing

Intensity Normalisation. Due to a difference of intensity values between subjects, we performed intensity normalisation using fuzzy C means-based normalisation, which normalises the intensity of the white matter (WM) [13].

For deriving WM mask, we used the Brain extraction tool (BET) form the FSL package [15] on T1-weighted images, with subsequent use of automated segmentation tool [17]. The patient data was processed in the patient native space.

Atlas Initialisation. Initial STN was presented as an atlas 3D mesh derived from Harvard Oxford subcortical atlas [16].

For positioning the atlas mesh into the native space, we used the manually expert-labelled STN landmarks (P1 and P2) and the posterior commissure (PC).

2.4 Active Contours Fitting

For adjusting the STN boundary, we used an active contour model (ACM), which can be described as snake model [9]. Snake model implement the idea of iterative

updates of a boundary curve $v(s) = (x(s), y(s), z(s))$ along the contour segment s, minimising the energy

$$E^*_{snake} = \int_0^1 E_{snake}(v(s))ds = \int_0^1 E_{int}(v(s)) + E_{image}(v(s)) + E_{con}(v(s))ds,$$

where E_{int} represents internal energy of bending spline, E_{image} is an energy represented by image forces, E_{con} represents constraints.

In the presented case of STN segmentation, where the boundary is not well defined by intensity gradient, we used a Chan-Vese model (CV) [5] whose stopping condition of curve evolution is not defined by the gradient but as the optimum of an energy function:

$$\begin{aligned} F(S, s_1, s_2) = \mu \cdot area(S) + v \cdot volume(insideS) \\ + \lambda_1 \int_{inside(S)} |I - s_1|^2 dxdydz \\ + \lambda_2 \int_{outside(S)} |I - s_2|^2 dxdydz, \end{aligned}$$

where I is the image, S is the surface, s_1 is the average intensity inside the surface and s_2 is average intensity outside the surface. The $\mu, v, \lambda_1, \lambda_2$ are the method parameters.

As the MRI data is coarse in terms of spatial resolution (i.e. large voxel size of the 1.5T data), while on the other hand the STN model is a triangular mesh with high level of detail, we modified the original method to work in the following way: We adapted the model from [10]:

$$V(S, s_1, s_2) = |\frac{dS(u)}{d\boldsymbol{n}}| \cdot (\lambda_1 \cdot |I - s_1|^2 + \lambda_2 \cdot |I - s_2|^2)$$

$$u = \begin{cases} 1 & if \quad V < 0, \text{ inside of the surface} \\ 0 & if \quad V \geq 0, \text{ outside of the surface,} \end{cases}$$

where S is optimisation surface, u is structure volume mask recalculated on each algorithm iteration, $\boldsymbol{n}$ is a vector of normal to the vertex of the mesh. We implemented this model with updating mesh vertices using gradients along vertex normals on each iteration. In each iteration, we thus updated the position of each vertex along the direction of its normal. The gradient along vertex normals was calculated using b-spline interpolation of voxel-based intensities.

After each iteration, we used a shape normalisation step, which prevents our vertices to go too close to each other and make them more uniformly distributed throughout the surface of the STN. In this constraint, we move each vertex in the direction of the largest adjacent mesh triangle, as suggested by [12].

As parameters of the CV model, we set λ_1 higher than λ_2, which made the variance of intensity inside of segmented volume lower than outside. We did not consider λ_1 and λ_2 being equal due to a marked difference in intensity values inside of STN and outside.

2.5 MER-based Fitting

In the next step, we shift the 3D STN contour, resulting from the segmentation, to fit the recorded electrophysiology. For this purpose, we use the parametric probabilistic model based on NRMS values, described previously in [1,2]. We search for a translation of the segmented STN volume (i.e. shift along the x, y and z axis) that minimises the negative log-likelihood of the atlas position with respect to the MER data:

$$t^* = arg\min_t \sum_{i=1}^{N} -\ln(p(\{x_i, l_i\}|t, \Theta))$$

where t* is the resulting translation vector along the x, y, z axes, x_i are the N NRMS values measured at locations l_i (i.e. the MER recording sites) and Θ are parameters of the probabilistic model estimated on training data. The resulting translation t^* is then applied to the STN model and evaluated. Contrary to the original work, no scaling or rotation was done at this stage.

2.6 Evaluation Procedure

In order to evaluate the performance of the presented model, including MER-based fitting, we used an iterative leave-one-subject-out (LOSO) cross-validation. In each iteration, all (i.e. one or two) trajectories of a single patient were kept for validation, while all remaining data were used for calculating model parameters. Once the procedure was finished for all subjects, the validation set performance was evaluated. The image-based segmentation using the modified Chan-Vese algorithm was completed prior to the LOSO procedure. A summary of the process at each iteration was as follows:

1. Train the parameters of the MER-based model using MER data of the current training $(N-1)$ subjects.
2. Perform the MER-based fit on the test subject using a) the landmark-initialised anatomical atlas, or b) the result of the modified Chan-Vese algorithm.

3 Results and Discussions

Here we present and evaluate the results of the active-contour border adjustment and electrode shifting and discuss limitations and future directions of the whole pipeline.

3.1 STN Segmentation

First, we analyse volumetric properties of the landmark-initialised atlas mesh (using the P1 and P2 points) and compare it with the mesh after the Chan-Vese segmentation. See the Table 1) which compares the result with previously published STN volumetric data [18].

We can see that the initialised volume is slightly lower compared to the reference values. This differences may be due to the similar intensity values in the border between STN and Substantia nigra (SNr) and issues in labelling. Additionally, the reference values [18] may yield different results than the classical MRI intensity-based segmentation.

Table 1. STN volumes measured for initialised model by manual labels and for Chan-Vese adjusted model

	Initialised atlas, mm^3	CV segmentation, mm^3	Reference [18], mm^3
Left	101.88 ± 45.07	101.10 ± 33.05	128.8 ± 17.10
Right	76.65 ± 21.47	132.14 ± 70.95	134.52 ± 22.82

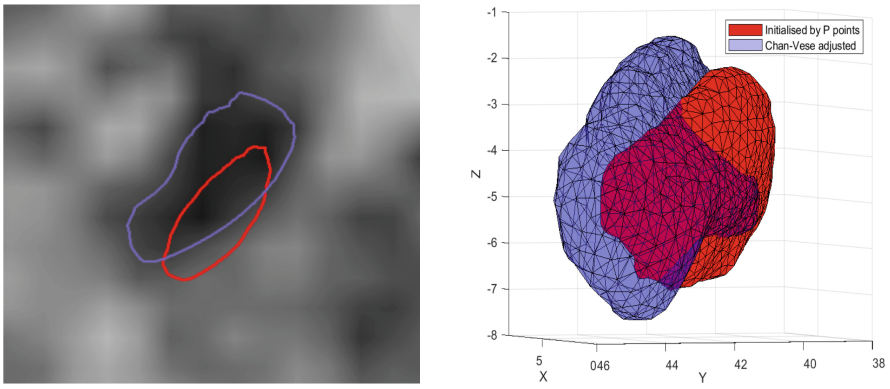

MRI T2 image 3D representation

Fig. 1. Both evaluated mesh representations: the landmark-initialised atlas (red) and the modified Chan-Vese segmentation (blue). The contours are shown overlaid over the T2 image (1a) and as a 3D representation (1b), both in the same patient (Color figure online)

For the Chan-Vese model, we observe that model fits well with the dorsolateral STN borders (see Fig. 1a), which are the primary targets during DBS surgery [7]. However, the observed standard deviation of segmented STN volumes is significantly higher from reference volumes which is the result of low

contrast in the anterior structure border. From results (see Fig. 1), we observed that CV algorithm partially include SNR into segmented volume.

To improve the segmentation results, we suggest to build a model with shape constraints and intensity modelling seems necessary, as was used in previous studies [12,16].

3.2 MER-based Fitting

The MER-based fitting represents the brain-shift correction by estimating the most likely STN shift according to the expected and observed electrophysiological activity. For evaluation, we used the expert labels of each MER recording as inside/outside of the STN and calculated the accuracy, sensitivity and specificity of correctly including/excluding each recording. The Youden's J index ($sensitivity + specificity - 1$) was calculated due to the high-class imbalance of the dataset with most recordings being from outside the STN. Table 2 and Fig. 2 present the values achieved by both surface models at their initial positions and after the MER fitting.

As seen from the results, the MER fitting improved the fit in both cases. The highest mean accuracy was achieved by the original atlas shape after MER fit, while the Chan-Vese segmentation achieved the best sensitivity and Youden's J index. This suggests the segmented STN shape better represents the individual characteristics of the highly variable STN nucleus. However, it may also be connected to the slightly higher volumes of the Chan-Vese segmentation, as discussed above.

The Fig. 3 shows the 3D situation with microelectrode recordings and initial and final fit of the atlas for both methods. It can be seen that the MER-based fitting correctly shifted both models so that the expert-labelled STN recordings (yellow electrode segments) are inside the final volume (recording locations marked by black dots).

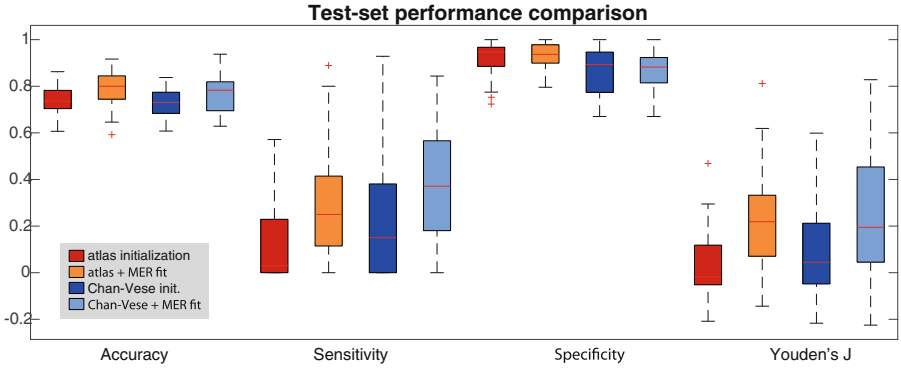

Fig. 2. Performance comparison of model location after the MER-based fitting. MER recording sites correctly included/excluded from the STN volume are considered as positive/negative examples, respectively.

Table 2. Performance evaluation of the MER-fitting results as mean (sd.), see also Fig. 2

Method	Accuracy	Sensitivity	Specificity	Youden's J
Atlas init	0.742 (0.062)	0.112 (0.151)	0.917 (0.073)	0.029 (0.136)
Atlas MERfit	0.794 (0.071)	0.283 (0.211)	0.930 (0.057)	0.214 (0.215)
CV init	0.726 (0.061)	0.233 (0.247)	0.865 (0.099)	0.098 (0.189)
CV MERfit	0.762 (0.077)	0.376 (0.241)	0.863 (0.085)	0.240 (0.239)

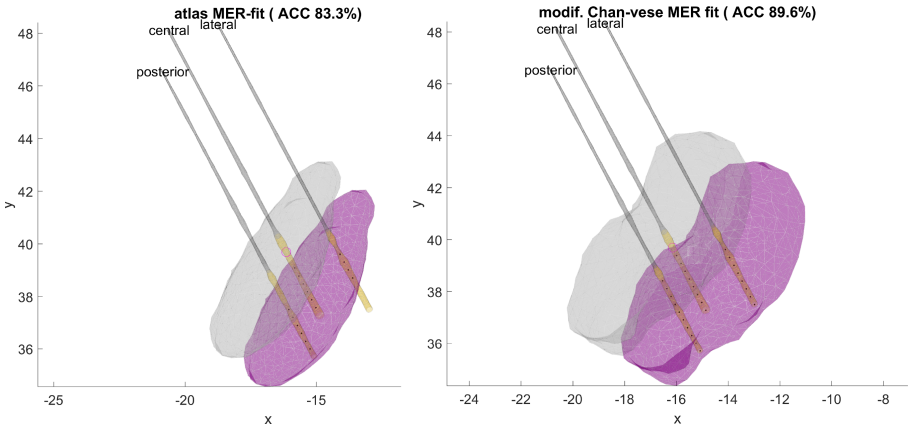

Fig. 3. MER-based fitting using the atlas surface model (left) and the modified Chan-Vese segmentation (right) for the same subject as in Fig. 1. The electrode trajectories are represented by the grey cylinders, the initial model position is shown in grey, the final one after MER fitting in violet. (Color figure online)

4 Conclusion

From the obtained results of STN segmentation, we see that the modified Chan-Vese model can fit the shape to the borders from MRI images, although it lacks in terms of shape constraints especially at the STN-SNR border, where the contrast is low. This can be improved by utilising the more sophisticated active shape and appearance models, which utilises probabilistic distribution fitting of the shape and intensity aspects of the nucleus [12,16]. The advantage of this approach is also the possibility to train several brain structures simultaneously and analyse statistical properties of shape and intensity in different positions. The other approach which could improve segmentation is training point distribution model using Deep Learning techniques which is useful in segmenting structures without prior information about other techniques.

Further, we observed that the estimation of the brain shift model could be used during surgery and allow surgeons more properly choose the target trajectory, as well as more accurately identify the MER recording sites in single-unit

studies concerning STN topology and its internal structure. This was allowed by utilisation of a rare data set combining MER and MRI data from the same subjects.

A major limitation of the presented results is the lack of ground-truth STN labels in our data set, which does not enable evaluation of the actual overlap between segmented and true STN. To provide a more accurate evaluation of the fit quality, manual expert evaluation of the STN contours will be necessary.

By combining the two approaches, the preoperative MRI-based segmentation of the individual STN shape, together with intra-operative MER-based improvement, may in the future provide unprecedented accuracy in 3D MER localisation and target identification during surgery.

Acknowledgments. The study was supported by the Research Centre for Informatics, grant number CZ.02.1.01/0.0/16˜019/0000765 and by the grant Biomedical data acquisition, processing and visualisation, number SGS19/171/OHK3/3T/13. The work of EB has been supported by the Ministry of Health of the Czech Republic under the grant NV19-04-00233.

References

1. Bakštein, E., Sieger, T., Novák, D., Růžička, F., Jech, R.: Automated atlas fitting for deep brain stimulation surgery based on microelectrode neuronal recordings. In: Lhotska, L., Sukupova, L., Lacković, I., Ibbott, G.S. (eds.) World Congress on Medical Physics and Biomedical Engineering 2018. IP, vol. 68/3, pp. 105–111. Springer, Singapore (2019). https://doi.org/10.1007/978-981-10-9023-3_19
2. Bakštein, E., Sieger, T., Růžička, F., Novák, D., Jech, R.: Fusion of microelectrode neuronal recordings and MRI landmarks for automatic atlas fitting in deep brain stimulation surgery. In: Stoyanov, D., et al. (eds.) CARE/CLIP/OR 2.0/ISIC - 2018. LNCS, vol. 11041, pp. 175–183. Springer, Cham (2018). https://doi.org/10.1007/978-3-030-01201-4_19
3. Bakštein, E., et al.: Methods for automatic detection of artifacts in microelectrode recordings. J. Neurosci. Meth. **290**, 39–51 (2017)
4. Bjerknes, S., et al.: Multiple microelectrode recordings in STN-DBS surgery for Parkinson's disease: a randomized study. Mov. Disord. Clin. Pract. **5**(3), 296–305 (2018)
5. Chan, T., Vese, L.: An active contour model without edges. In: Nielsen, M., Johansen, P., Olsen, O.F., Weickert, J. (eds.) Scale-Space 1999. LNCS, vol. 1682, pp. 141–151. Springer, Heidelberg (1999). https://doi.org/10.1007/3-540-48236-9_13
6. Chen, X., Williams, B.M., Vallabhaneni, S.R., Czanner, G., Williams, R., Zheng, Y.: Learning active contour models for medical image segmentation. In: 2019 IEEE/CVF Conference on Computer Vision and Pattern Recognition (CVPR), pp. 11624–11632. IEEE, Long Beach, CA, USA, June 2019
7. Coenen, V.A., Prescher, A., Schmidt, T., Picozzi, P., Gielen, F.L.H.: What is dorsolateral in the subthalamic Nucleus (STN)?–a topographic and anatomical consideration on the ambiguous description of today's primary target for deep brain stimulation (DBS) surgery. Acta Neurochir. (Wien) **150**(11), 1163–1165 (2008)

8. Groiss, S., Wojtecki, L., Südmeyer, M., Schnitzler, A.: Review: deep brain stimulation in Parkinson's disease. Ther. Adv. Neurol. Disord. **2**(6), 379–391 (2009)
9. Kass, M., Witkin, A., Terzopoulos, D.: Snakes: active contour models. Int. J. Comput. Vision **1**(4), 321–331 (1988)
10. Marquez-Neila, P., Baumela, L., Alvarez, L.: A morphological approach to curvature-based evolution of curves and surfaces. IEEE Trans. Pattern Anal. Mach. Intell. **36**(1), 2–17 (2014)
11. Moran, A., Bar-Gad, I., Bergman, H., Israel, Z.: Real-time refinement of subthalamic nucleus targeting using Bayesian decision-making on the root mean square measure. Mov. Disord. **21**(9), 1425–1431 (2006)
12. Patenaude, B., Smith, S.M., Kennedy, D.N., Jenkinson, M.: A Bayesian model of shape and appearance for subcortical brain segmentation. NeuroImage **56**(3), 907–922 (2011)
13. Reinhold, J.C., Dewey, B.E., Carass, A., Prince, J.L.: Evaluating the impact of intensity normalization on MR image synthesis. arXiv:1812.04652 [cs], December 2018. arXiv: 1812.04652
14. Sieger, T., et al.: Distinct populations of neurons respond to emotional valence and arousal in the human subthalamic nucleus. Proc. Natl. Acad. Sci. **112**(10), 3116–3121 (2015)
15. Smith, S.M.: Fast robust automated brain extraction. Hum. Brain Mapp. **17**(3), 143–155 (2002)
16. Visser, E., Keuken, M.C., Forstmann, B.U., Jenkinson, M.: Automated segmentation of the substantia nigra, subthalamic nucleus and red nucleus in 7 T data at young and old age. Neuroimage **139**, 324–336 (2016)
17. Zhang, Y., Brady, M., Smith, S.: Segmentation of brain MR images through a hidden Markov random field model and the expectation-maximization algorithm. IEEE Trans. Med. Imaging **20**(1), 45–57 (2001)
18. Zwirner, J., et al.: Subthalamic nucleus volumes are highly consistent but decrease age-dependently-a combined magnetic resonance imaging and stereology approach in humans. Hum. Brain Mapp. **38**(2), 909–922 (2017)